# Detailed investigation of the local flow-field in a Wells turbine coupled to an OWC simulator

Fabio Licheri[a,*], Tiziano Ghisu[a], Francesco Cambuli[a], Pierpaolo Puddu[a]

[a]*Department of Mechanical, Chemical and Materials Engineering. University of Cagliari, via Marengo 2, 09123 Cagliari, Italy*

**Abstract**

One of the most promising technologies for sea-wave energy conversion is the one based on the OWC principle. In a system of this type, the oscillatory motion of the sea waves is converted into a bi-directional air flow which is commonly exploited by means of a self-rectifying turbine such as the Wells turbine, the simplest and most reliable device for this purpose. The vast majority of experiments on Wells turbines and OWC devices has analyzed their performance from a global point of view, often in experimental facilities where the turbine was operated under stationary flow conditions.

This paper presents the results of the experimental investigation carried out on a Wells turbine, by measuring the flow field both upstream and downstream of the rotor, in a laboratory set-up capable to reproduce the bi-directional air-flow typical of an OWC system. The investigation aims to evaluate the local performance of the Wells turbine under unsteady flow conditions.

The experimental measurements allow the identification of the loss components that affect the performance of the turbine. Viscous losses, due to the aerodynamic of the rotor cascade, represent the main contribution to the total losses, and appear larger than kinetic energy losses at the machine exhaust.

*Keywords:* OWC systems, Wells turbines, experimental analysis, aerodynamic probes, turbine efficiency, components of loss

## 1. Introduction

The large availability and predictability [1] of ocean wave power, globally estimated in about 3.7 TW [2], contribute to make it highly attractive as a renewable source. Researches on technologies and devices capable to harvest and convert wave energy into electrical energy, conducted during the last four decades, have proposed several solutions and modifications to improve the most promising designs [3].

Among the technical solutions proposed, systems based on Oscillating Water Column (OWC) principle have attracted researchers for their simplicity and low environmental impact, especially in the case of

*Corresponding author: fabio.licheri@unica.it

plants located near- or on-shore [4]. Electrical energy production with OWC devices is generally obtained through two conversion stages, starting from the potential energy contained in wave motion: the former was a chamber (partially submerged under the free water surface) to convert the wave motion into pneumatic energy in the form of a bi-directional airflow of a mass of air; then, a power-take-off, generally an air turbine, converts the energy contained in the periodic airflow into shaft energy.

The bi-directional nature of the airflow inside the OWC represents a challenge in turbine selection. Traditional turbines, such as impulse turbines, are consolidated machines, but they need rectification systems to be coupled with the OWC, such as pneumatic valves or stator blades on both sides of the rotor [5, 6, 7, 8]. More recently, bi-radial turbines have been proposed for this scope [9]. Among the different types of turbines proposed and studied [10], the Wells turbine invented by Dr. A. A. Wells in 1980s [11] is the simplest one in virtue of its self-rectifying nature due to the symmetrical profiles of its blades. Its simplicity of construction and reliability have attracted a number of researchers, who investigated turbine performance both with numerical [12, 13, 14, 15] and experimental [16, 17, 18, 19] approaches.

Experimental analyses have been conducted in laboratories using unidirectional rigs [18, 20, 21] or, with a more representative approach, OWC simulators [16, 17, 19, 22]. Both approaches have focused on characterizing the turbine's performance, i.e. output torque, pressure drop across the rotor and then turbine efficiency, generally aiming to compare different turbine geometries and control strategies in order to obtain optimal performance, often expressed in terms of maximum output torque or mean efficiency. On the contrary, only local flow analyses can properly lead the search of improved solutions for turbine and stationary parts. Experimental works present in the scientific literature, related to local investigations of the flow in a Wells turbine, are quite rare and refer mainly to steady-state flow conditions. The local flow analyses presented in [21] compare measurements with numerical predictions for different turbine solidities. In a recent work [23], local flow measurements along the blade height have been conducted in a uni-directional rig in order to compare the aerodynamic behavior of a bi-plane Wells turbine with and without guide vanes.

This paper presents a local flow analysis for a Wells turbine coupled with an OWC simulator housed in the Department of Mechanical, Chemical and Materials Engineering (DIMCM) at the University of Cagliari [16, 17]. The experimental investigation has been conducted using aerodynamic pressure probes, in order to reconstruct the flow field near the turbine blades, at different radial positions. The experimental measurements have been used to characterize the specific Wells turbine tested, in terms of global and local performance, in order to highlight the regions where higher losses are located, as well as their intensity. Overall losses have been decomposed in two main components, i.e. viscous loss and exit kinetic energy loss, following an analytical approach in order to evaluate their relative influence on rotor efficiency.

Several recent works [24, 25] have shown that the turbine's non-dimensional frequency inside an OWC system is about 1-2 orders of magnitude lower than the typical values required to observe dynamic effects

in lifting surfaces [26, 27] (i.e. hysteresis). This means that the measurements performed under non-stationary operating conditions, as in the present work, will not differ from the ones performed under stationary conditions, as in [28]. The main advantage of conducting the measurements in an OWC simulator is the capability to investigate the full operating range, from maximum flow during inflow to maximum flow during outflow, with a significant reduction of test duration. This is especially true when probe traversing is performed for the local flow measurements.

In the first part of this manuscript, the investigation methodology has been presented with a focus on the definition of global and local performance parameters adopted. Using established thermo-fluid dynamics relations, an analytical procedure was developed in order to identify and highlight the main contributions to the overall losses occurring through the turbine. Then, the experimental rig and instrumentation have been described with particular attention to the aerodynamic pressure probe used in the investigation. The central part of the article presents the results in terms of global and local performance parameters. A conclusion summarizes the results and presents some considerations to guide future turbine performance improvements.

## 2. Methodology

### *2.1. Performance parameters*

The common Wells turbine's global performance parameters are the flow coefficient $\phi$, the aerodynamic torque coefficient $T^*$ and the wall pressure drop coefficient $p^*$, defined in Eqn. (1).

$$\phi = \frac{C_z}{\Omega r_{tip}} \qquad T^* = \frac{T}{\rho \Omega^2 r_{tip}^5} \qquad p^* = \frac{\Delta p}{\rho \Omega^2 r_{tip}^2} \tag{1}$$

The static pressure drop $\Delta p$ is measured with wall pressure taps placed upstream and downstream of the rotor. The axial velocity component $C_z$ is evaluated from piston motion with a phase-lag correction to account for the capacitive effect of the chamber [29, 30, 31], while the aerodynamic torque $T$ is obtained from the measured torque at the turbine shaft, corrected to account for inertia and windage contributions. Dimensionless parameters defined in Eqn. (1) can be readily calculated by means of global measurements.

As in a Wells turbine the exhaust kinetic energy is entirely wasted [15, 32, 33], its efficiency is more appropriately calculated with reference to the outlet static conditions:

$$\eta_{ts} = \frac{T\Omega}{(P_1 - p_2)\, Q} \tag{2}$$

During the inflow phase, the total pressure at turbine's inlet $P_1$ can be approximated with the atmospheric pressure, if inlet duct pressure losses are neglected. This assumption simplifies the efficiency calculation, which can be rearranged as follows:

$$\eta_{ts} = \frac{T^*}{p^*\,\phi} \cdot \frac{1}{\pi\,(1-\nu^2)} \tag{3}$$

In order to identify the loss components that affect the efficiency of a Wells turbine, it can be useful to consider the enthalpy-entropy diagram in Fig. 1.

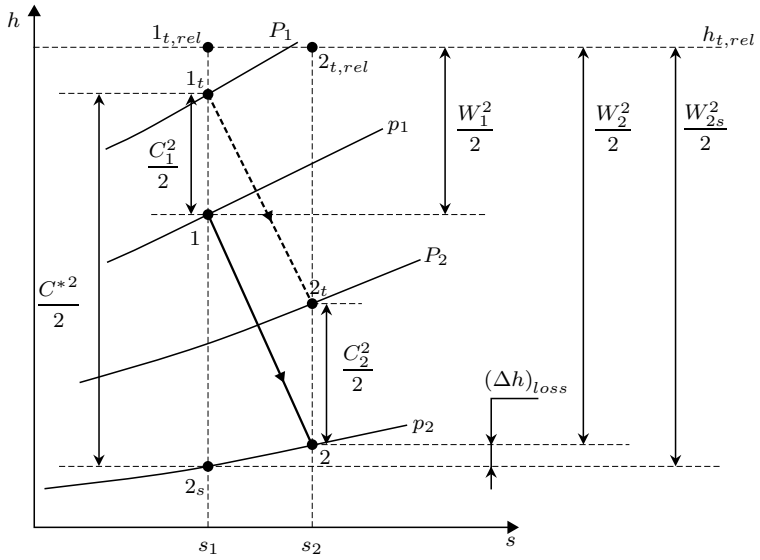


Figure 1: Expansion through the Wells rotor in the $h-s$ diagram.

Considering the total available energy $h_{1t} - h_{2s}$, represented by the isentropic expansion $1_t \to 2_s$, and the output work $h_{1t} - h_{2t}$, represented by the real expansion $1_t \to 2_t$, the *total-to-static* efficiency can be expressed as follows:

$$\eta_{ts} = \frac{h_{1t} - h_{2t}}{h_{1t} - h_{2s}} = \frac{h_{1t} - h_{2t} + h_{2s} - h_2 + h_2 - h_{2s}}{h_{1t} - h_{2s}} = 1 - \frac{C_2^2/2}{h_{1t} - h_{2s}} - \frac{(\Delta h)_{loss}}{h_{1t} - h_{2s}} = 1 - \xi_{EX} - \xi_R \tag{4}$$

where $\xi_R$ and $\xi_{EX}$ are the loss coefficients related to viscous losses and exit kinetic energy, respectively. The reference velocity $C^*$ (representatives of the available work) can be introduced as shown in Fig. 1. Also, the loss of enthalpy $(\Delta h)_{loss}$ can be expressed in terms of relative velocities:

$$(\Delta h)_{loss} = h_2 - h_{2s} = \frac{{W_{2s}}^2 - W_2^2}{2} = \frac{{W_{2s}}^2}{2}\left(1-\psi^2\right) \tag{5}$$

where $\psi = W_2/W_{2s}$ is the reduction coefficient for the relative velocity and $W_{2s}$ can be determined from measurements as shown in Appendix A. Then, the rotor loss coefficient $\xi_R$ can be rewritten based on Eqn. (5), introducing the velocity coefficient $\lambda = U/C^*$:

$$\xi_R = \frac{(\Delta h)_{loss}}{h_{1t} - h_{2s}} = \left(1-\psi^2\right)\left(\frac{W_{2s}}{U}\right)^2 \lambda^2 \tag{6}$$

Common velocity triangles at inlet and outlet of the rotor, as reported in Fig. 2, are helpful to express $\xi_R$ as a function of flow angles, rather than velocities. Then

$$\xi_R = \left(1 - \psi^2\right)\left(1 + \lambda^2 - 2\phi\lambda^2 \cot \alpha_1\right) \tag{7}$$

where the flow coefficient $\phi$ can be derived from the velocity inlet triangle in Fig. 2 as follows:

$$\phi = \frac{C_1 \sin(\alpha_1)}{U} \tag{8}$$

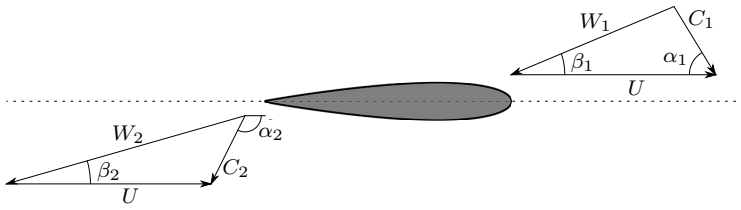


Figure 2: Velocity triangles at inlet and outlet of a Wells turbine.

Following the same approach, with the help of the velocity triangles in Fig. 2, it is possible to derive a similar expression for the exit loss coefficient $\xi_{EX}$:

$$\xi_{EX} = \frac{C_2^2/2}{h_{1t} - h_{2s}} = \lambda^2 + \psi^2\left(1 + \lambda^2 - 2\lambda^2\phi\cot\alpha_1\right) - 2\psi\lambda\cos\beta_2\left(1 + \lambda^2 - 2\lambda^2\phi\cot\alpha_1\right)^{1/2} \tag{9}$$

Finally, the *total-to-static* efficiency can be expressed as a function of the flow angles $\alpha_1$ and $\beta_2$ and of the non-dimensional parameters $\lambda$, $\psi$ and $\phi$:

$$\eta_{ts} = 2\lambda^2\left[\phi\cot\alpha_1 - 1 + \frac{\psi\cos\beta_2}{\lambda}\left(\lambda^2 + 1 - 2\lambda^2\phi\cot\alpha_1\right)^{1/2}\right] \tag{10}$$

The expressions for efficiency, Eqn. (10), and loss coefficients, Eqns. (7) and (9), can be simplified assuming the inlet flow to be axial, i.e. $\alpha_1 = 90°$, as typical for a Wells turbine inside an OWC when the airflow comes from the atmosphere.

$$\left.\begin{aligned} \xi_R &= \left(1 - \psi^2\right)\left(1 + \lambda^2\right) \\ \xi_{EX} &= \lambda^2 + \psi^2\left(1 + \lambda^2\right) - 2\psi\lambda\cos\beta_2\sqrt{1 + \lambda^2} \\ \eta_{ts} &= 2\lambda\left(\psi\cos\beta_2\sqrt{1 + \lambda^2} - \lambda\right) \end{aligned}\right\} \; for \;\; \alpha_1 = 90° \tag{11}$$

From Eqn. (11), it is clear that rotor losses depends on $\lambda = U/C^*$ and $\psi$, which are related to the operating conditions and aerodynamic losses, while they are independent from the deviation angle $\beta_2$ which only affects the discharge loss coefficients $\xi_{EX}$, instead. This consideration becomes important because the Wells turbine works under variable flow conditions, as the unsteady flow conditions determine

continuous, albeit slow [24], variation of the $U/C^*$ parameter. In order to keep the efficiency as high as possible, it is necessary for the turbine to work in the vicinity of the conditions for which $\lambda = U/C^*$ determines the maximum efficiency: due to the fact that $C^*$ continuously changes, one way to achieve this is by controlling the peripheral speed $U$.

Aside the traditional performance parameters reported in Eqn. (1) and the *total-to-static* efficiency, see Eqn. (2), it is interesting to introduce two additional coefficients that can be useful to characterize the local performance of the Wells rotor. The first parameter is the *relative total pressure loss* coefficient $Y_P$ defined by [34] as follows:

$$Y_P = \frac{P_{1,rel} - P_{2,rel}}{1/2 \rho_2 W_2^2} \tag{12}$$

$Y_P$ represents a measure of the aerodynamic losses through the rotor [35] and it can be related to the velocity reduction coefficient $\psi$ (see Appendix B) through the following expression:

$$Y_P = \frac{1}{\psi^2} - 1 \tag{13}$$

By coupling Eqns. (13) and (11), the rotor loss $\xi_R$ can be expressed as a function of the aerodynamic performance, $Y_P$:

$$\xi_R = \left( \frac{Y_P}{Y_P + 1} \right) \left( 1 + \lambda^2 \right) \tag{14}$$

This expression shows that $\xi_R$ is affected only by the aerodynamic losses through the cascade, weighted with the operating conditions of the turbine $(1 + \lambda^2)$.

Finally, a second important parameter is the work coefficient $\varphi$, which represents the specific work $l$ non-dimensionalized with respect to the peripheral velocity:

$$\varphi = \frac{l}{U_{tip}^2} = \frac{U \left( C_{1\theta} - C_{2\theta} \right)}{U_{tip}^2} \tag{15}$$

*2.2. Experimental apparatus and instrumentation*

Figure 3 shows a schematic view of the experimental rig. It consists of a chamber made of steel where a hydraulic control unit drives a piston generating a periodic bi-directional airflow. Piston motion's amplitude and period can be adjusted to regulate the flow speed. A linear potentiometer measures the piston position during its motion and is used for feedback control in the hydraulic unit.

The piston motion has been set to be sinusoidal by fixing its amplitude and period, as reported in Tab. 1, and its non-dimensional position $Z^*$, defined in Eqn. (16), is reported in Fig. 4 as a function of the non-dimensional period $t/T_w$.

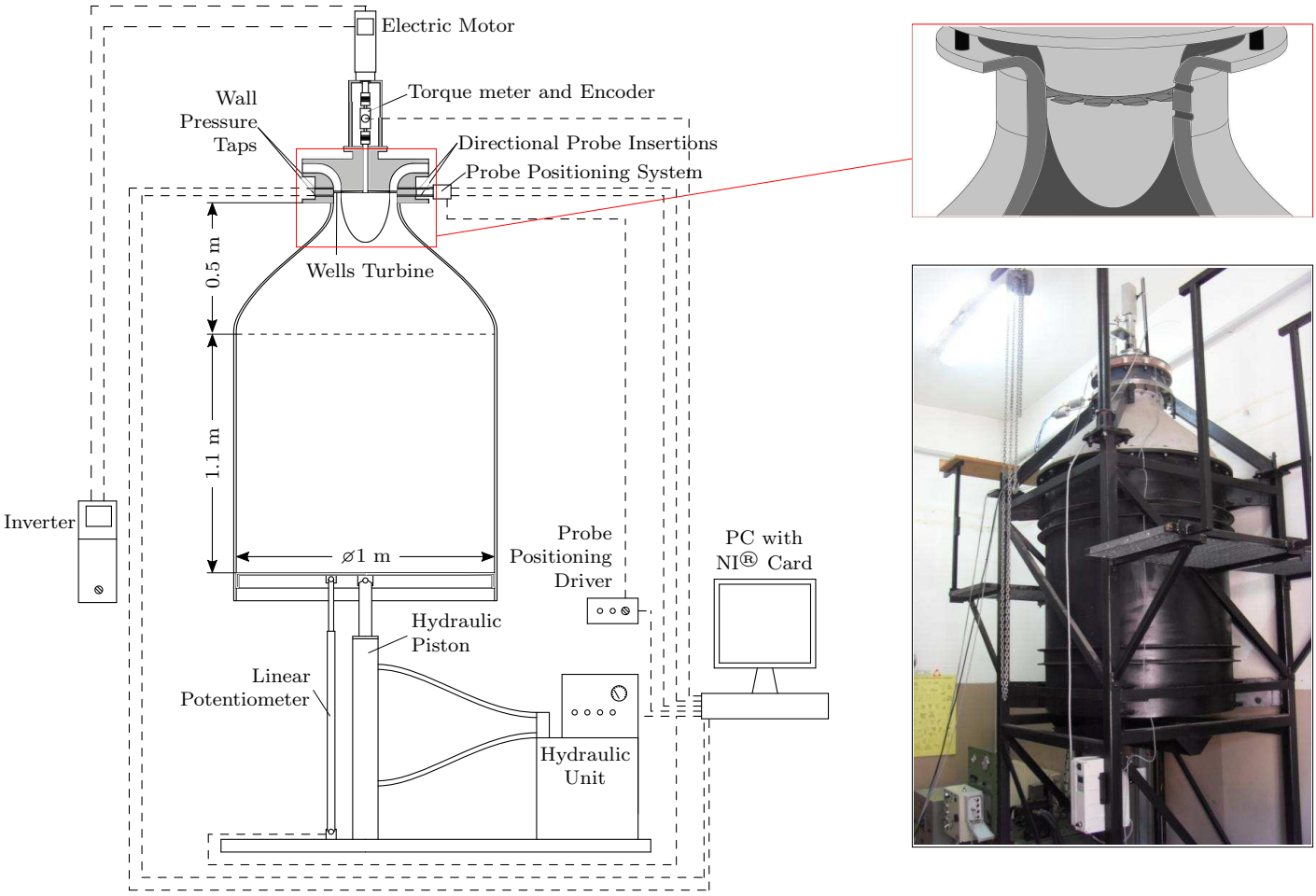


Figure 3: Schematic view of the experimental rig with a close-up view of the turbine.

$$Z^* = \frac{z - z_{min}}{z_{max} - z_{min}} \tag{16}$$

Table 1: Settings of the experiment

| | |
|---|---|
| Turbine rotational speed, $n$ | 3600 rpm |
| Piston stroke amplitude, $z_{max} - z_{min}$ | 900 mm |
| Piston period, $T_w$ | 9 s |
| Reynolds' number of the outlet flow based on blade chord, $Re$ | $\approx 1.3\times10^5$ |
| Maximum relative Mach number of the outlet flow, $M$ | $\approx 0.2$ |

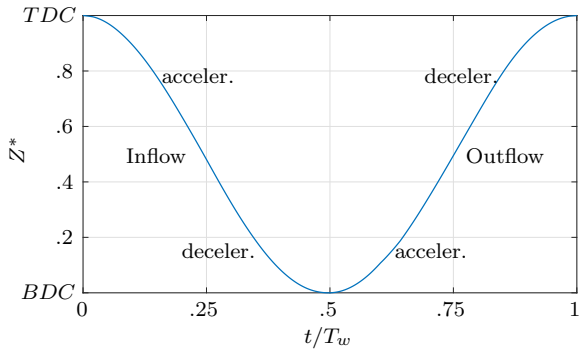


Figure 4: Non-dimensional piston motion used in the tests.

The motion parameters have been set in order to simulate a regular wave and to obtain incipient stall conditions at the maximum flow coefficient. Only one value of the piston period has been selected in the present investigations, as no dynamics effects were expected for the aerodynamic behavior of the turbine.

In the top section of the steel chamber, a high solidity Wells turbine is housed. The turbine drives an induction motor controlled by an inverter with encoder feedback. A close-up view of the turbine connected with the motor is shown inside the red square in Fig. 3, while its main geometric characteristics are summarized in Tab. 2.

Table 2: Wells turbine data

| | |
|---|---|
| Rotor tip diameter, $D_{tip}$ | 250 mm |
| Rotor hub diameter, $D_{hub}$ | 190 mm |
| Tip clearance | 1 mm |
| Chord length, $c$ | 36 mm |
| Sweep ratio | 0.417 (15/36) |
| Number of blades | 14 |
| Airfoil profile | NACA0015 |
| Solidity, $\sigma$ | 0.729 |
| Hub-to-tip ratio, $\nu$ | 0.76 |

The tested Wells turbine has been designed in order to obtain an area ratio of 38 between the piston surface and the turbine duct area. This value ensures a flow speed between 10 - 20 m/s, based on the adjustable motion parameters, which is typical for Wells turbine coupled to OWC systems, assuming a rotational frequency of 60 Hz. With this hub-to-tip ratio, the rotor solidity has been selected to guarantee the self-starting behavior of the turbine accordingly to [36] (this was important when the rig was designed, while the use of an inverter to start the turbine now overcomes this requirement).

A torque meter, placed in between the turbine shaft and the motor, is used to perform torque mea-

surements, while the rotational speed is measured thanks to the built-in optical encoder. The torque meter operating range is equal to $\pm 2$ Nm with a maximum measurement uncertainty of 0.1% of full scale.

Flow investigations have been conducted by means of pressure measurements. Wall pressure taps have been placed both at ambient and piston sides of the experimental set-up, about $\pm 7.5$ mm away from the turbine symmetry plane. Near-rotor flow characterization has been performed using a 3-holes aerodynamic probe both at turbine inlet and outlet. Flow reconstruction has been conducted with the aerodynamic probe, under the assumption of a two-dimensional flow field, i.e. neglecting the radial velocity component. The latter can be assumed small when compared to axial and tangential components, especially upstream of the rotor [17]. The probe has been designed to minimize distortion effects on the flow field, considering the small turbine blade height, in order to perform a fine scan of the pressure distribution along the blade span. Two sets of pressure transducers with different operating ranges have been selected, depending on the turbine side (piston chamber or ambient side). The radial traversing is produced by a motorized system.

A personal computer equipped with a National Instruments multifunction DAQ-board and MATLAB scripts has been used to control the probe position and perform data acquisition. The turbine's speed has been set to avoid stall at the maximum flow speed, and has been kept constant by the inverter's PID controller. In this way, the maximum output torque is expected for the maximum flow coefficient, where near stall conditions will be reached and the incidence flow angle will be the largest.

The acquisition time for each probe position has been set to record signals for at least 5 piston periods. This allows to obtain an average distribution of the quantities along a piston period, by applying the phase locked averaging process to the acquired signals for consecutive periods. 18 radial positions are distributed along the blade span with a higher resolution near the walls, where larger pressure gradients were expected. For each probe position, global measurements have also been carried out, i.e. wall-static pressure both up- and down-stream the rotor, output torque, piston position and turbine rotational speed. Data acquisition has been been performed with a sampling rate of 1 kHz for all the acquired signals. Based on the instrumentation measurement uncertainties, calibration methods, uncertainty propagation and other influencing variables (such as mounting positions of the sensors), the maximum uncertainties of the measured variables can be estimated as follows:

- 0.3% and 0.2% of full scale for the wall pressure measurements at ambient and piston side, respectively (where the full scale is 1000 Pa for the ambient side transducer and 6895 Pa for the piston side one);
- 0.1% of full scale for the torque sensor;
- $\pm 1$ mm for the piston position.

Measurements repeatability, evaluated by means of different tests carried out in several days, are:

- 2.5 mm for the piston position, which leads to a measurement repeatability of about 5 mm/s for the calculation of the piston velocity;
- 40 Pa for the wall static pressure drop.

These uncertainties have been obtained from Figs. 5 (a), (b) and (c), where the values of these three parameters for tests carried out in successive days are shown. The piston velocity is calculated from its instantaneous position.

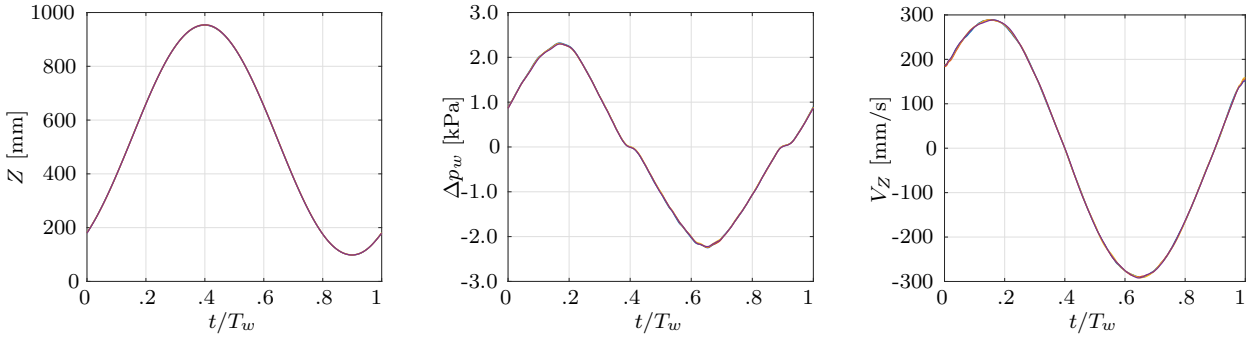


(a) Piston position. (b) Wall static pressure drop. (c) Piston velocity.

Figure 5: Measured quantities in successive tests as a function of the non-dimensional period.

### *2.3. Aerodynamic Probe*

A miniaturized "Cobra" probe has been used for local flow reconstruction. Figure 6 (a) shows the probe geometry, identifying its pressure taps, while Fig. 6 (b) reports a schematic view of probe positioning at turbine inlet and outlet. Detailed pictures of the probe are also shown in 6 (c) and (d).

The probe's head has a maximum dimension in the radial direction of about 1 mm, thus allowing a fine scan resolution along the blade span and ensuring a fast response. The aerodynamic probe has been used in "non-nulling" mode within its angular calibration range, in order to determine the flow angle on the tangential plane and total and static pressures. Probe orientations have been selected based on the expected flow directions both at the inlet and at the outlet of the turbine. The angular calibration has been conducted in a subsonic wind tunnel, by relating the pressures measured by the probe holes indicated in Fig. 6 (a) with the true values, i.e. the total pressure $P$ and the static pressure $p$, and the flow angle, as follows:

$$K_Y = \frac{p_l - p_r}{q_{ref}} \qquad K_T = \frac{P - p_f}{P - p} \qquad K_S = \frac{p - (p_l + p_r)/2}{P - p} \tag{17}$$

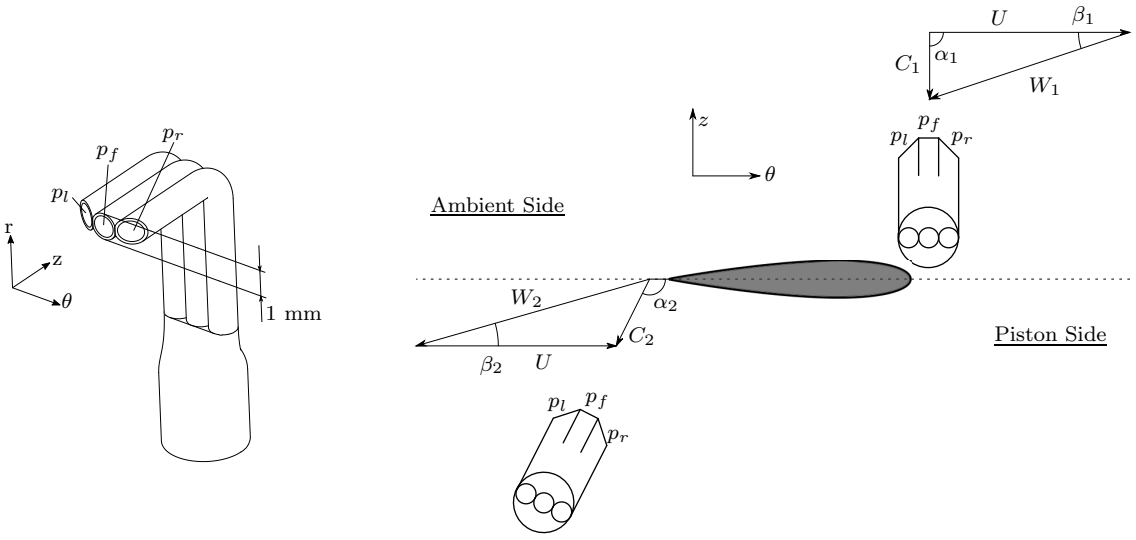


(a) Probe geometry.

(b) Probe orientations.

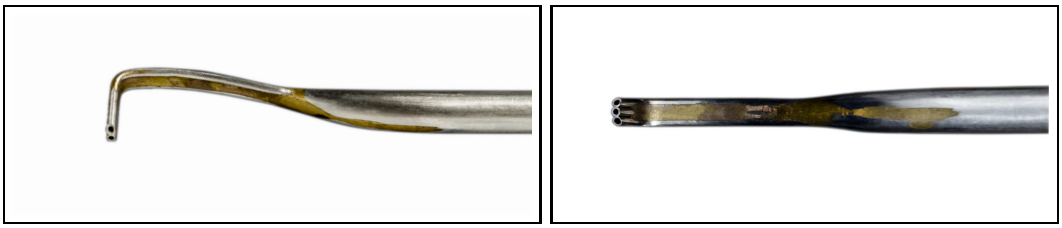

(c) Side view of the probe.

(d) Front view of the probe.

Figure 6: Probe configuration and positioning upstream and downstream the rotor during the inflow phase.

where $K_Y$, $K_T$ and $K_S$ represent the yaw coefficient and the total and static pressure coefficients, respectively; $q_{ref}$ represents the "dynamic pressure" of the probe, calculated as $p_f - (p_l + p_r)/2$. The calibration coefficients defined in Eqn. (17) allow to determine flow pressures and yaw angle, directly. Figure 7 shows their values as evaluated during the calibration process.

During testing, starting from the pressure probe measurements ($p_l$, $p_r$ and $p_f$), $K_Y$ is calculated as in Eqn. (17), and the yaw angle is determined from Fig. 7 (a). Then, $K_T$ and $K_S$ are known from Fig. 7 (b), based on the yaw angle, and total, $P$, and static, $p$, pressures are calculated using Eqns. (17).

The calibration of the 3-holes probe was carried out in a free-jet wind tunnel. The maximum uncertainties of the measured variables, considering also the interpolation process, are: $\pm 30$ Pa for the total pressure; $\pm 40$ Pa for the static pressure; $\pm 0.5°$ for the yaw angle.

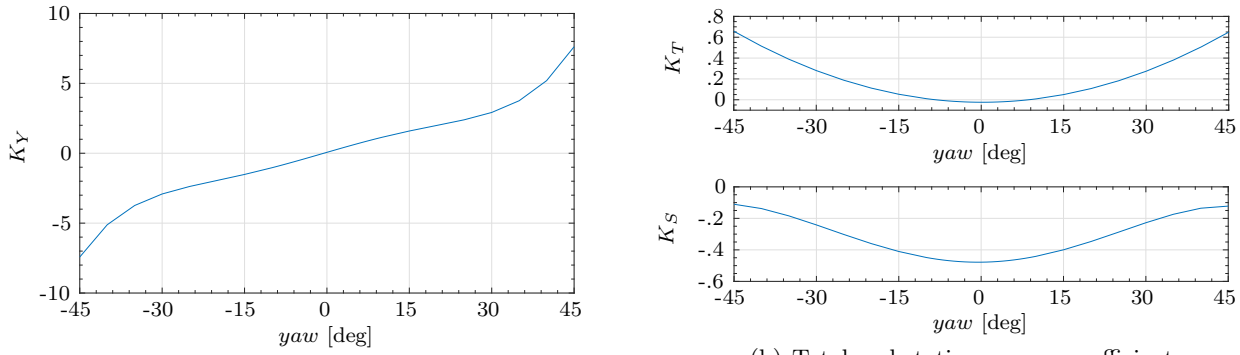


(a) Yaw coefficient.

(b) Total and static pressure coefficients.

Figure 7: Calibration curves for the "Cobra" probe.

## 3. Results and discussion

### *3.1. Local measurements*

The detailed analysis of the local flow field is performed during the inflow phase, as flow characteristics do not present significant differences during the outflow phase.

In order to present the measurements performed with the "Cobra" probe, total and static pressures have been non-dimensionalized with respect to a reference kinetic energy, as expressed in Eqn. (18).

$$C_P = \frac{P - p_a}{\frac{1}{2}\rho_a U_{tip}^2} \qquad C_p = \frac{p - p_a}{\frac{1}{2}\rho_a U_{tip}^2} \tag{18}$$

In Figs. 8 and 9, probe measurements have been reported at three spanwise positions, $r^*$, as a function of the non-dimensional piston position, $Z^*$, upstream and downstream of the rotor, respectively.

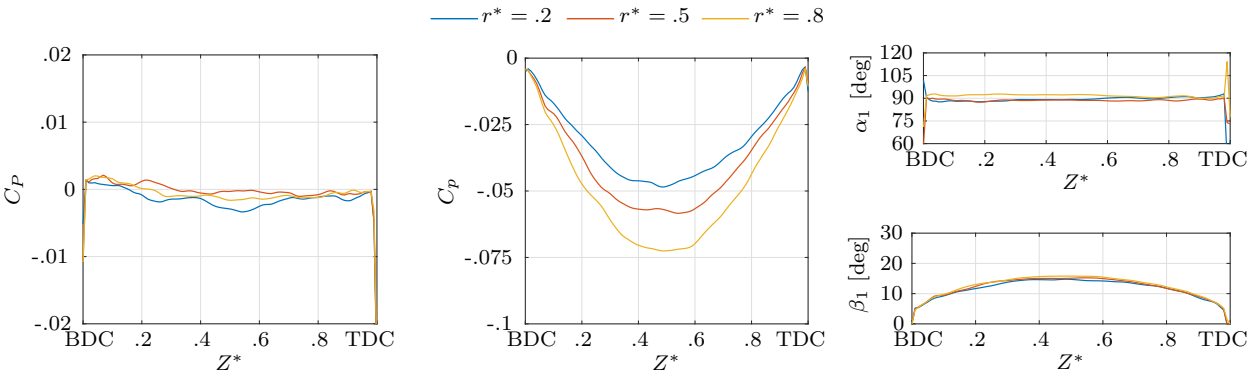


(a) Non-dimensional total pressure.

(b) Non-dimensional static pressure.

(c) Flow angles.

Figure 8: Measurements of the "Cobra" probe at turbine's inlet, as a function of the piston position at three spanwise positions (inflow phase).

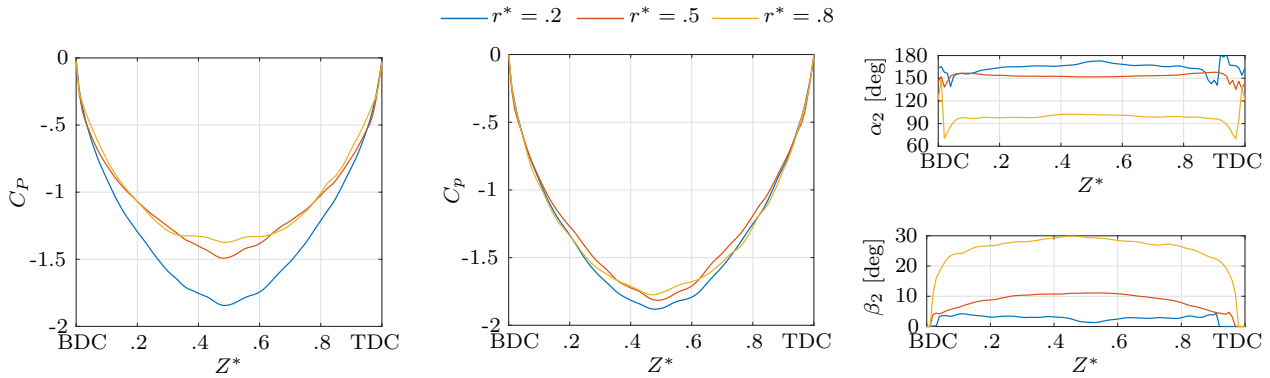


(a) Non-dimensional total pressure. (b) Non-dimensional static pressure. (c) Flow angles.

Figure 9: Measurements of the "Cobra" probe at turbine's outlet, as a function of the piston position at three spanwise positions (inflow phase).

Local measurements at turbine's inlet show an almost axial absolute flow, see $\alpha_1$ in Fig. 8 (c), at every radial position during the entire inflow phase. The total pressure is approximately equal to the ambient value, $p_a$, and constant for every flow condition and radial position, as expected, while the static pressure has a gradient along the blade span, due to the presence of the curved duct. The large axial velocity towards the tip of the blade, combined with a larger blade speed, determines the same distribution of relative flow angle $\beta_1$ at the three radial positions. The turbine's outlet flow, reported in Fig. 9, is characterized by large gradients of flow angles, both for $\alpha_2$ and $\beta_2$, along the blade span. In particular, the absolute flow angle $\alpha_2$, in the hub region, is characteristic of an almost tangential absolute flow and a very small axial velocity component: the high solidity of the rotor at the hub determines a strong blockage of the flow (total, Fig. 9 (a), and static, Fig. 9 (b), pressures attain almost the same value). At this radial position, the deviation angle attains very small values, due to the reduced axial velocity component. On the contrary, the absolute flow in the tip region is almost axial due to the strong influence of the leakage flow, and the deviation angle is larger than at other radial positions. The leakage flow affects a relatively large portion of the blade height as it is still noticeable at 80% of the blade span.

### *3.2. Global performance analysis*

Turbine global performance, expressed in Eqns. (1) and (2), are reported in Fig. 10 as a function of the flow coefficient $\phi$.

Non-dimensional parameters' trends show that in the tested working conditions no turbine stall occurs. As expected, the static pressure drop coefficient increases monotonically with the flow coefficient similarly to the torque coefficient, as the tests were conducted at operating conditions free from stall. Figure 10 (c) highlights the best efficiency condition for $\phi \approx 0.2$, after which the *total-to-static* efficiency of the turbine starts to decrease again. No differences can be observed between acceleration and deceleration

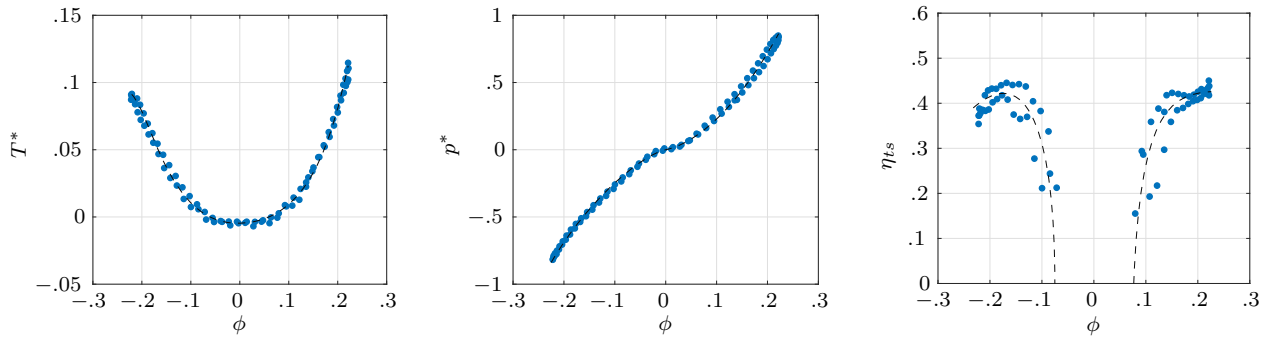


(a) Non-dimensional torque coefficient. (b) Non-dimensional static pressure drop. (c) *Total-to-static* efficiency.

Figure 10: Wells turbine performance parameters as a function of the flow coefficient.

phases, as well known from literature [25], given the low non-dimensional frequency, of about $3{\cdot}10^{-4}$. This confirms that Wells turbine's performance can be measured also with steady-state experiments, although one-directional rigs do not allow to observe the differences between inflow and outflow phases, as shown for the non-dimensional torque in Fig. 10 (a). These are due to the presence in the outflow phase of a swirling flow generated by the previous inflow phase, as discussed in detail in [16].

Global performance parameters, presented in Fig. 10, are obtained considering only global measurements, and they give an overall picture of the aerodynamic behavior of the turbine, without any indication of local rotor contributions to global performance.

### *3.3. Local performance analysis*

In order to investigate the contribution of different blade regions to the global performance, the contour plots of the *relative total pressure loss* coefficient $Y_P$ and the work coefficient $\varphi$, as a function of the non-dimensional radius $r^*$ and piston position $Z^*$, are reported in Fig. 11. These graphical representations show the local performance of the Wells turbine for the different flow conditions experienced during its typical unsteady operation.

Performance parameters $Y_P$ and $\varphi$ are symmetric with respect to the middle piston position between TDC and BDC, i.e. $Z^* = 0.5$, which means that they do not change during accelerating and decelerating phases. This result confirms the same conclusions obtained from global performance measurements, with the additional information that the symmetric behavior is preserved all along the blade span. The *relative total pressure loss* coefficient $Y_P$, in Fig. 11 (a), presents lower values around the midspan region at all flow conditions, represented by the piston position $Z^*$. Higher values can be observed in the tip region and near the hub, where the effects of leakage and blockage, respectively, determine higher losses in terms of relative total pressure. The same consideration can be drawn by looking at the contour plot in Fig. 11 (b), which represents the work coefficient of the turbine as defined in Eqn. (15). Most of the work

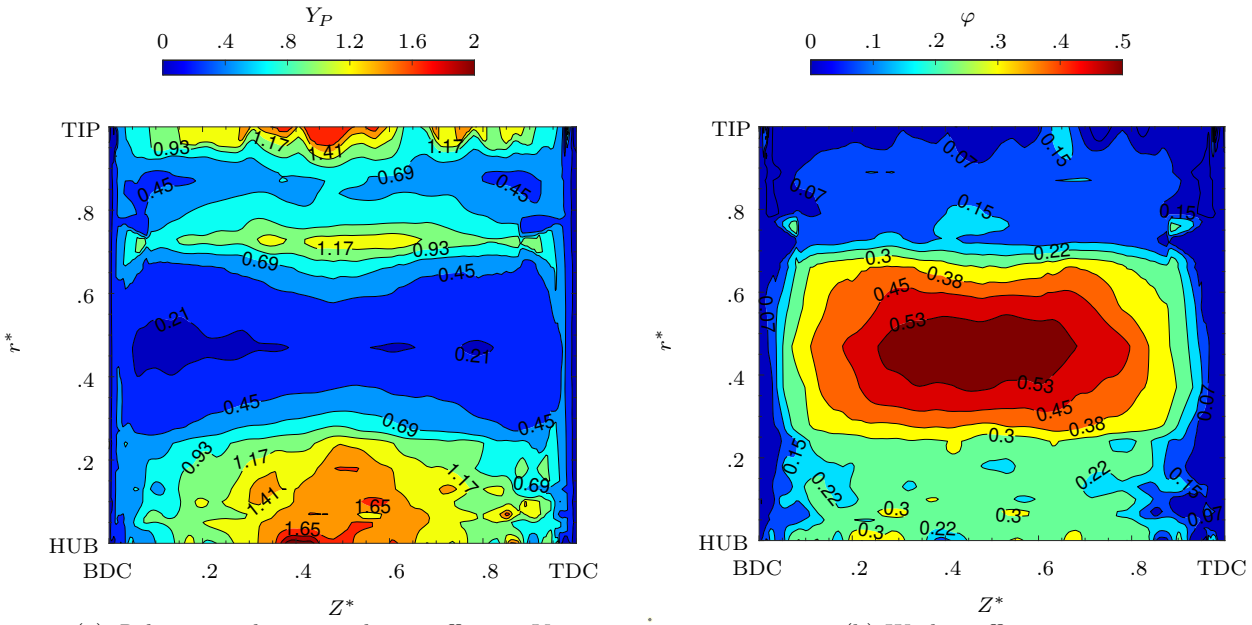


(a) *Relative total pressure loss* coefficient, $Y_P$ (b) Work coefficient, $\varphi$

Figure 11: Contour plots of turbine performance parameters.

produced by the rotor is localized around the blade midspan region at every flow condition, with the exception of conditions near the inversions of piston motion ($Z^* \approx 0$ and $Z^* \approx 1$), where performance is clearly poor all along the blade span. Contours show that tip leakage and blockage affect a relatively large portion of the blade span and this is due to the high *hub-to-tip* ratio of the blade. In the midspan region, where aerodynamic losses are the lowest, the *relative total pressure loss* coefficient $Y_P$ does not change significantly during the piston displacement, meaning that rotor aerodynamic performance are almost independent from operating conditions in the absence of other effects, such as high blockage and leakage.

Local contributions, in terms of turbine loss coefficients, are also presented for the whole turbine rotor, at the different operating conditions experienced during the test. Figures 12 (a) and (b) report contours of loss coefficients $\xi_R$ and $\xi_{EX}$, respectively, as a function of the non-dimensional radius $r^*$ and piston position $Z^*$.

The symmetric distribution of losses with respect to the middle piston position appears clear, as well as expected given the results presented in Fig. 11, especially at midspan. The rotor loss coefficient $\xi_R$ highlights a better rotor behavior around the midspan region for a wide range of flow conditions (different $Z^*$ values). Rotor losses appear larger at the tip, due to the leakage flow, and in the hub region, due to the strong blockage effect. In the tip region, most of the losses are due to the exit kinetic energy (larger values of $\xi_{EX}$) because a considerably part of the flow rate passes in this region, where the rotor solidity is the lowest. Considerations on loss localization suggest a reduction in rotor solidity at the blade root

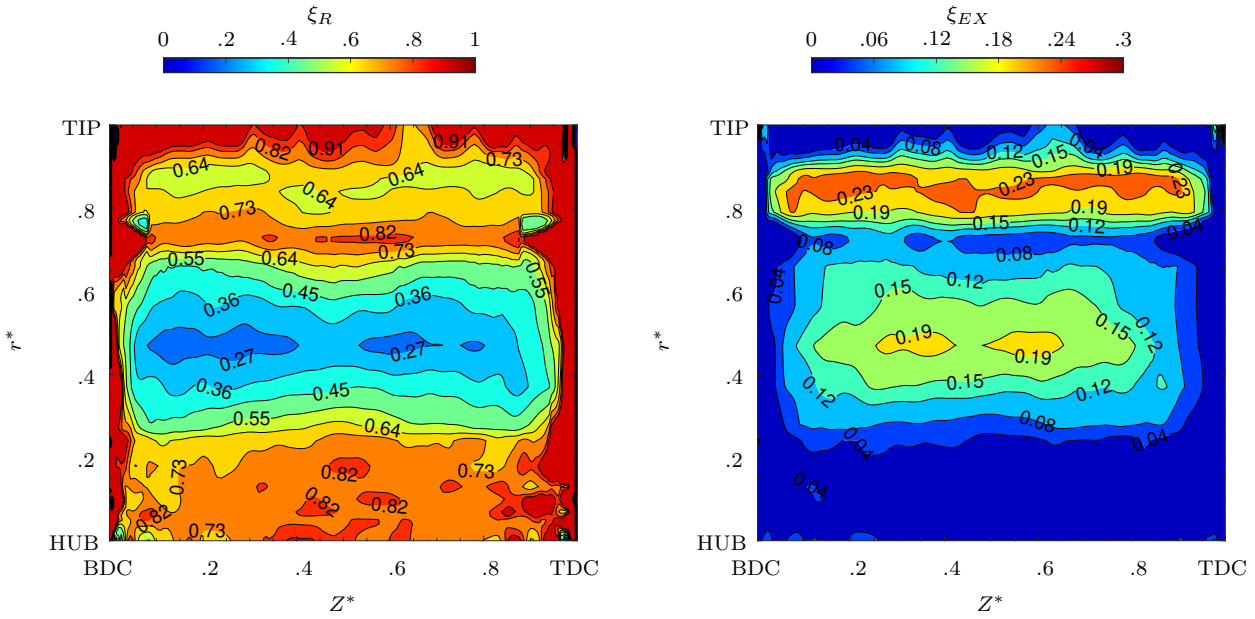


(a) Rotor losses. (b) Exit losses.

Figure 12: Components of losses of the turbine.

to mitigate the blockage effect, while a lower *hub-to-tip* ratio could reduce the relative importance of tip leakage and hub interaction effects.

Finally, it is interesting to show the relative influence of the two loss coefficients, as a function of the incidence angle $\beta_1$ and of the velocity coefficient $U/C^*$, Fig. 13 (a) and (b), respectively.

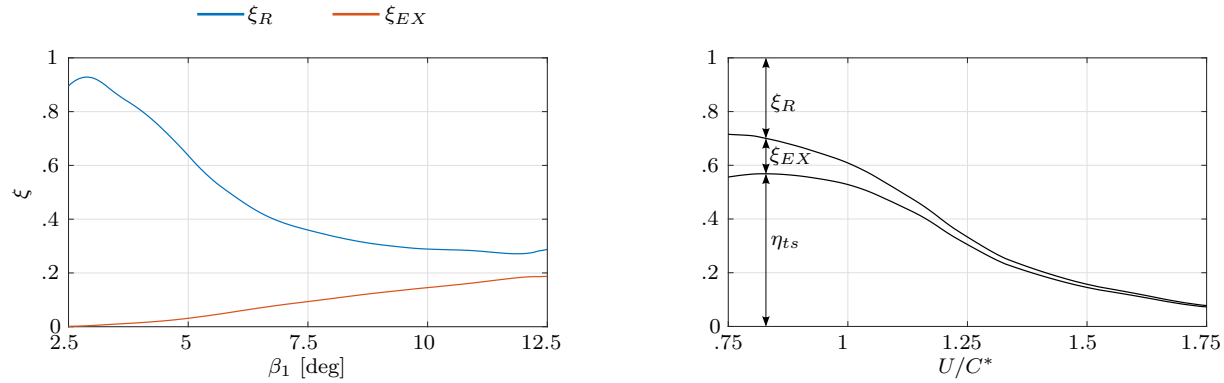


(a) Loss coefficients as a function of the angle of incidence. (b) Efficiency decomposition as a function of the velocity coefficient.

Figure 13: Loss coefficients of the turbine at blade midspan.

It appears clear that rotor aerodynamic loss coefficient $\xi_R$ is always larger than exit kinetic energy loss coefficient $\xi_{EX}$, for every flow condition (see Fig. 13 (a)). The former decreases with the incident angle, but it can be assumed almost constant in a region between $\beta_1 = 10 \div 12$ degrees, that represents

the optimal incidence range for the rotor. Conversely, the latter always grows with the incidence angle as the flow rate increases. The relative influence of the loss coefficients on the rotor efficiency is clarified in Fig. 13 (b), where $\xi_R$ and $\xi_{EX}$, calculated at midspan, are plotted with respect to the velocity coefficient $U/C^*$. In the tested case, $\beta_2$ changes with the operating conditions, Fig. 9 (c), as wells as $\psi$, that attains different values with the operating conditions, as reported in Fig 14.

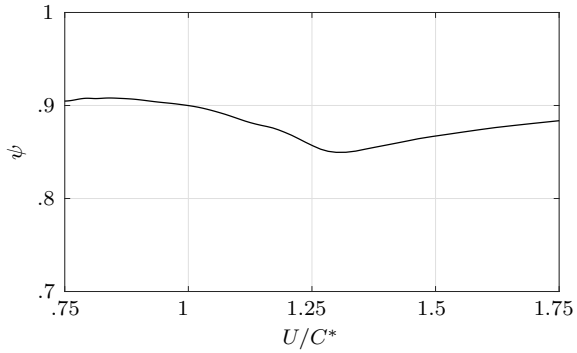


Figure 14: Velocity reduction coefficient as a function of the operating conditions.

These graphs confirm that the losses inside the Wells turbine are mainly due to the rotor losses that increase significantly at operating conditions away from the optimal operating condition, and only a relative small amount of losses can be related to the exit kinetic energy.

These results, reported as an example in Figs. 13, are evaluated at the midspan region. Similar graphs can be obtained for different radial stations along the blade span, using the data reported in Fig. 12, and the considerations made for the midspan position can be extended to other radial positions.

## 4. Conclusions

This paper presents the results of an experimental investigation on the local flow field upstream and downstream a Wells turbine coupled with an Oscillating Water Column simulator. Tests have been carried out under unsteady and periodic bi-directional air-flow representative of the normal operation of an OWC plant. Aerodynamic pressure probes have been used to reconstruct the local flow-field inside the turbine, under the assumption of bi-dimensional airflow, as supported by previous results reported in the literature. Measured quantities have been used to calculate global and local performance, with particular attention to turbine efficiency and loss components. The results of this experimental investigation can be summarized as follows:

a. Most of the losses during the expansion through the Wells rotor are due to viscous losses in the rotor (aerodynamic efficiency) under unsteady conditions, in particular when the incidence is small, i.e. below 12 degrees, which corresponds to the optimal operating range. The losses due to the exit

kinetic energy grows with the flow rate, as expected, while rotor losses decrease, but the former is always lower than the latter.

b. The high solidity of the rotor at the hub strongly affects its performance, due to the strong blockage, responsible of poor local performance.

c. Low performance has been detected near the tip region of the blade due to the presence of leakage flow. This affects a relevant region of the blade height from tip to almost 30% of the blade span due to the high *hub-to-tip* ratio value.

The local evaluation of loss components helps to understand the reasons behind their global values and then gives a more detailed explanation of performance results. It suggests that particular attention needs to be paid to the rotor losses since they are the main driver for rotor efficiency. A reduction in rotor solidity, especially in the hub region, and a lower *hub-to-tip* ratio are two modifications that could be applied to improve the design of the analyzed Wells turbine. Nevertheless, unsteady operating conditions are intrinsically responsible for losses when the turbine works away from its optimal efficiency range. The turbine rotational speed could be controlled in order to keep operating conditions closer to maximum efficiency.

Last but not least, this paper provides experimental results on the entire flow field downstream of the Wells turbine which represents an important database for a more precise verification of numerical simulations.

## Appendix A. Calculation of the relative velocity $W_{2s}$

Starting from the expansion through the Wells rotor represented on the $h-s$ diagram, see Fig. 1, the isentropic relative velocity $W_{2s}$ can be evaluated as follows:

$$\frac{W_{2s}^2}{2} = \frac{W_1^2}{2} + (h_1 - h_{2s}) = \frac{W_1^2}{2} + \frac{C^{*2} - C_1^2}{2} \tag{A.1}$$

where the reference velocity $C^*$ can be practically calculated knowing the pressure of the flow field. In fact

$$\frac{C^{*2}}{2} = h_{t1} - h_{2s} = \int_{t_1}^{2} \frac{\mathrm{d}p}{\rho} \tag{A.2}$$

and, assuming the air density to be constant with respect to the inlet conditions, i.e. $\rho = \rho_1 = const$, the reference velocity $C^*$ can be simply evaluated from the static wall pressure measurements.

$$\frac{C^{*2}}{2} \approx \frac{P_1 - p_2}{\rho_1} \tag{A.3}$$

Then, considering the velocity triangle at the inlet of the Wells rotor, see Fig. 2, it is possible to express Eqn. (A.1) as follows:

$$\frac{W_{2s}^2}{2} = \frac{\cancel{C_1^2}}{\cancel{2}} + \frac{U^2}{2} - UC_1\cos\alpha_1 + \frac{C^{*2}}{2} - \frac{\cancel{C_1^2}}{\cancel{2}} = \frac{U^2}{2} - U^2\phi\cot\alpha_1 + \frac{C^{*2}}{2} \tag{A.4}$$

where all the quantities, except the reference velocity $C^*$, can be determined from flow field measurements. Finally, Eqn. (A.4) can be simplified assuming the inlet flow to be axial, i.e. $\alpha_1 = 90°$, as proposed in Sec. 2.

$$\frac{W_{2s}^2}{2} = \frac{U^2}{2} + \frac{C^{*2}}{2} \tag{A.5}$$

## Appendix B. Calculation of the *total pressure loss* coefficient $Y_P$

The calculation of $Y_P$, as defined in Eqn. (12), requires total pressures of the relative flow $P_{rel}$. Considering transformations in the diagram of Fig. 1, points $1_{t,rel}$ and $2_s$ lie on an isentropic line as for points $2_{t,rel}$ and 2. Then, using Gibbs' equation and assuming the flow to be incompressible, it is possible to write:

$$\begin{cases} h_{t1,rel} - h_{2s} = \dfrac{P_{1,rel} - p_2}{\rho} \\ h_{t2,rel} - h_2 = \dfrac{P_{2,rel} - p_2}{\rho} \end{cases} \tag{B.1}$$

where the total enthalpy of the relative flow, i.e. the *rothalpy*, can be calculated as in Eqn. (B.2) and it is preserved during the transformation through a rotor [35].

$$h_{t,rel} = h + \frac{W^2}{2} - \frac{U^2}{2} = cost \implies \begin{cases} h_{t1,rel} = h_{2s} + \dfrac{W_{2s}^2}{2} - \dfrac{U^2}{2} \\ h_{t2,rel} = h_2 + \dfrac{W_2^2}{2} - \dfrac{U^2}{2} \end{cases} \tag{B.2}$$

Then, Eqn. (12) can be combined with Eqns. (B.1) and (B.2) in order to express the *relative total pressure loss* coefficient as a function velocity components.

$$Y_P = \frac{W_{2s}^2 - W_2^2}{W_2^2} = \frac{1}{\psi^2} - 1 \tag{B.3}$$

## References


[1] R. Pelc, R. Fujita, Renewable energy from the ocean, Marine Policy 26 (6) (2002) 471–479. doi:10.1016/S0308-597X(02)00045-3.

[2] Assessing the Global Wave Energy Potential, Vol. 29th International Conference on Ocean, Offshore and Arctic Engineering: Volume 3 of International Conference on Offshore Mechanics and Arctic Engineering. doi:10.1115/OMAE2010-20473.

[3] T. Aderinto, H. Li, Ocean wave energy converters: Status and challenges, Energies 11 (5). doi:10.3390/en11051250.

[4] A. Falcão, Wave energy utilization: A review of the technologies, Renewable and Sustainable Energy Reviews 14 (3) (2010) 899–918. doi:10.1016/j.rser.2009.11.003.

[5] Z. Liu, Y. Cui, C. Xu, L. Sun, M. Li, J. Jin, Experimental and numerical studies on an owc axial-flow impulse turbine in reciprocating air flows, Renewable and Sustainable Energy Reviews 113 (2019) 109272. doi:https://doi.org/10.1016/j.rser.2019.109272.

[6] M. Takao, T. Setoguchi, Air turbines for wave energy conversion, International Journal of Rotating Machinery 2012.

[7] T. Setoguchi, S. Santhakumar, H. Maeda, M. Takao, K. Kaneko, A review of impulse turbines for wave energy conversion, Renewable Energy 23 (2) (2001) 261–292. doi:https://doi.org/10.1016/S0960-1481(00)00175-0.

[8] Y. Masuda, An Experience of Wave Power Generator through Tests and Improvement, In: Evans D.V., de Falcão A.F.O. (eds) Hydrodynamics of Ocean Wave-Energy Utilization. International Union of Theoretical and Applied Mechanics. Springer, Berlin, Heidelberg, 1986. doi:https://doi.org/10.1007/978-3-642-82666-5-36.

[9] A. Carrelhas, L. Gato, J. Henriques, A. Falcão, J. Varandas, Test results of a 30 kW self-rectifying biradial air turbine-generator prototype, Renewable and Sustainable Energy Reviews 109 (2019) 187–198. doi:https://doi.org/10.1016/j.rser.2019.04.008.

[10] A. Falcão, J. Henriques, Oscillating-water-column wave energy converters and air turbines: A review, Renewable Energy 85 (2016) 1391–1424. doi:10.1016/j.renene.2015.07.086.

[11] A. Wells, Fluid Driven Rotary Transducer - BR. Pat. 1595700 (1976).

[12] T. Dhanasekaran, M. Govardhan, Computational analysis of performance and flow investigation on Wells turbine for wave energy conversion, Renewable Energy 30 (14) (2005) 2129–2147. doi:10.1016/j.renene.2005.02.005.

[13] M. Torresi, S. Camporeale, P. Strippoli, G. Pascazio, Accurate numerical simulation of a high solidity Wells turbine, Renewable Energy 33 (4) (2008) 735 – 747. doi:10.1016/j.renene.2007.04.006.

[14] T. Ghisu, P. Puddu, F. Cambuli, A detailed analysis of the unsteady flow within a wells turbine, Proceedings of the Institution of Mechanical Engineers, Part A: Journal of Power and Energy 231 (3) (2017) 197–214. doi:10.1177/0957650917691640.

[15] F. Licheri, F. Cambuli, P. Puddu, T. Ghisu, A comparison of different approaches to estimate the efficiency of Wells turbines, Journal of Fluids Engineering 143 (5). doi:10.1115/1.4049686.

[16] P. Puddu, M. Paderi, C. Manca, Aerodynamic characterization of a Wells turbine under bi-directional airflow, Energy Procedia 45 (2014) 278–287. doi:10.1016/j.egypro.2014.01.030.

[17] M. Paderi, P. Puddu, Experimental investigation in a wells turbine under bi-directional flow, Renewable Energy 57 (2013) 570–576. doi:10.1016/j.renene.2013.02.016.

[18] R. Curran, L. M. C. Gato, The energy conversion performance of several types of Wells turbine designs, Proceedings of the Institution of Mechanical Engineers, Part A: Journal of Power and Energy 211 (2) (1997) 133–145. doi:10.1243/0957650971537051.

[19] A. Thakker, R. Abdulhadi, The performance of Wells turbine under bi-directional airflow, Renewable Energy 33 (11) (2008) 2467 – 2474. doi:0.1016/j.renene.2008.02.013.

[20] M. Torresi, M. Stefanizzi, F. Fornarelli, L. Gurnari, P. G. F. Filianoti, S. M. Camporeale, Performance characterization of a wells turbine under unsteady flow conditions, AIP Conference Proceedings 2191 (1) (2019) 020149. doi:10.1063/1.5138882.

[21] L. Gato, A. de O. Falcão, Aerodynamics of the Wells turbine, International Journal of Mechanical Sciences 30 (6) (1988) 383 – 395. doi:10.1016/0020-7403(88)90012-4.

[22] T. K. Das, K. Kumar, A. Samad, Experimental analysis of a biplane wells turbine under different load conditions, Energy 206 (2020) 118205. doi:https://doi.org/10.1016/j.energy.2020.118205.

[23] J. S. Alves, L. M. Gato, A. F. Falcão, J. C. Henriques, Experimental investigation on performance improvement by mid-plane guide-vanes in a biplane-rotor wells turbine for wave energy conversion, Renewable and Sustainable Energy Reviews 150 (2021) 111497. doi:https://doi.org/10.1016/j.rser.2021.111497.

[24] T. Ghisu, P. Puddu, F. Cambuli, Physical Explanation of the Hysteresis in Wells Turbines: A Critical Reconsideration, Journal of Fluids Engineering 138 (11), 111105. doi:10.1115/1.4033320.

[25] T. Ghisu, F. Cambuli, P. Puddu, I. Virdis, M. Carta, F. Licheri, A critical examination of the hysteresis in wells turbines using computational fluid dynamics and lumped parameter models, Journal of Offshore Mechanics and Arctic Engineering 142 (5). doi:10.1115/1.4046379.

[26] L. W. Carr, K. W. McAlister, W. J. McCroskey, Analysis of the development of dynamic stall based on oscillating airfoil experiments, Tech. Rep. NASA Technical Note D-8382, NASA AMES Research Center (1977).

[27] K. W. McAlister, L. W. Carr, M. W. J., Dynamic Stall Experiements on the NACA 0012 Airfoil, Tech. Rep. NASA Technical Paper 1100, NASA (1978). doi:10.1007/BF00575335.

[28] M. Torresi, M. Stefanizzi, L. Gurnari, P. G. F. Filianoti, S. M. Camporeale, Experimental characterization of the unsteady performance behavior of a wells turbine operating at high flow rate coefficients, E3S Web of Conferences 197 (2020) 08009. doi:10.1051/e3sconf/202019708009.

[29] T. Ghisu, P. Puddu, F. Cambuli, I. Virdis, On the hysteretic behaviour of Wells turbines, Energy Procedia 126 (2017) 706–713. doi:10.1016/j.egypro.2017.08.303.

[30] F. Cambuli, T. Ghisu, I. Virdis, P. Puddu, Dynamic interaction between OWC system and Wells turbine: A comparison between cfd and lumped parameter model approaches, Ocean Engineering 191 (2019) 106459. doi:10.1016/j.oceaneng.2019.106459.

[31] T. Ghisu, F. Cambuli, P. Puddu, I. Virdis, M. Carta, F. Licheri, A lumped parameter model to explain the cause of the hysteresis in OWC-Wells turbine systems for wave energy conversion, Applied Ocean Research 94 (2020) 101994. doi:10.1016/j.apor.2019.101994.

[32] S. Raghunathan, C. P. Tan, O. O. Ombaka, Performance of the Wells self-rectifying air turbine, Aeronautical Journal 89 (1985) 369–379.

[33] L. M. C. Gato, A. F. d. O. Falcão, On the theory of the Wells turbine, Journal of Engineering for Gas Turbines and Power 106 (3) (1984) 628–633. doi:10.1115/1.3239616.

[34] J. Horlock, Losses and efficiencies in axial-flow turbines, International Journal of Mechanical Sciences 2 (1) (1960) 48–75. doi:https://doi.org/10.1016/0020-7403(60)90013-8.

[35] S. L. Dixon, C. A. Hall, Fluid Mechanics and Thermodynamics of Turbomachinery, 6th Edition, Elsevier, Inc., 2010.

[36] S. Raghunathan, A methodology for Wells turbine design for wave energy conversion, Proceedings of the Institution of Mechanical Engineers, Part A: Journal of Power and Energy 209 (3) (1995) 221–232. doi:10.1243/PIME_PROC_1995_209_040_02.